significant fractions of material lost by the massive stars that had produced those anti-correlations must have been mixed with the pristine gas in the young GC before the low-mass stars formed out of that mixture.

Three types of H-burning in stars have been proposed as possible sources of the primordial abundance variations of p-capture elements in GCs: hot-bottom burning in massive asymptotic giant branch (AGB) stars (D'Antona, Gratton & Chieffi 1983), H burning in convective cores of rapidly rotating massive MS stars (Decressin et al. 2007) and, more recently, core H burning in supermassive MS stars with masses $M \gtrsim 10^4\,M_\odot$ (Denissenkov & Hartwick 2014). Fast rotation with a nearly break-up velocity in the second case plays a twofold role: firstly, it drives rotation-induced mixing in the radiative envelope, thus bringing H-burning products from the convective core to the surface and, secondly, it leads to equatorial mass loss with a relatively low velocity caused by the centrifugal force. The second property, like the assumed low-velocity mass loss by the AGB stars, is required to explain the retention of the mass lost by the massive stars in the shallow potential well of the young GC. It is also assumed that the massive AGB and MS stars had migrated to the GC centre, as a result of dynamical friction, before they deposited the products of H burning to the GC interstellar medium. The last assumption is usually used to interpret the larger fraction of low-mass stars with the stronger abundance anomalies in the cores of some GCs (e.g. Milone et al. 2012).

A solution of the problem of the primordial abundance variations in GCs should be divided into two steps. The first step is to find the right massive star candidate, such that when we dilute its H-burning yields with the GC pristine gas we get individual abundances and correlations between them consistent with all the relevant observational data for GCs. The second step is to understand how the required massive stellar objects formed and functioned, how their lost mass was retained and mixed with the pristine gas in GCs, and how significant fractions of low-mass stars made out of those gas mixtures survived and got distributed among their unpolluted counterparts in GCs by the present day.

We think that it is not worth discussing any solution details pertaining to the second step until the first step is completed, especially, given that there are a lot of observational data on abundances of p-capture elements and their isotopes in GC stars to constrain the solution on the first step, whereas there are no direct observational data on the formation of the first generation stars in GCs.

In this paper, we conclude that the massive AGB and MS stars are not the best candidates for the origin of the primordial abundance variations in GCs, because they fail to reproduce the correlations between the abundances of Al and Mg isotopes, that have recently been reported by Da Costa, Norris & Yong (2013) and now include stars from 5 GCs. We demonstrate that this failure is a consequence of temperatures of H burning in these objects that are either too high (in the case of AGB stars) or too low (in the case of massive MS stars). On the other hand, the hypothetical supermassive MS stars with $M \gtrsim 10^4\,M_\odot$ have the right temperature to nicely reproduce not only the Mg-Al anti-correlation, but also all the other observed abundance anomalies of the p-capture elements in GCs, including enhanced He abundances (Denissenkov & Hartwick 2014).

The primordial variations of the C and N abundances and $^{12}C/^{13}C$ isotopic ratio in GCs are obscured by their evolutionary changes that occur in low-mass stars, both in GCs and in the field, on the upper red giant branch (RGB) above the bump luminosity. These changes are caused by some extra mixing that operates in radiative zones of RGB stars between the H-burning shell (HBS) and the bottom of the convective envelope (BCE). It results in the decreasing surface C abundance and $^{12}C/^{13}C$ ratio and increasing N abundance when the star climbs the upper RGB and its luminosity increases. At the bump luminosity, the HBS, advancing in mass, erases a mean molecular weight (μ) discontinuity left behind by the BCE at the end of the first dredge-up. This discontinuity probably prevents extra mixing from reaching the HBS on the lower RGB. Above the bump luminosity, the μ-profile in the radiative zone is uniform everywhere, except the vicinity of the HBS, where the reaction ^{3}He(^{3}He,2p)^{4}He produces its local depression of the order of $\Delta\mu \sim 10^{-4}$ (Eggleton, Dearborn & Lattanzio 2006). This μ-depression should drive thermohaline mixing that was proposed for the role of RGB extra mixing by Charbonnel & Zahn (2007) who assumed that its associated fluid parcels ("salt fingers") had a ratio of their vertical length to horizontal diameter $a = l/d \approx 6.2$. However, numerical simulations of thermohaline convection by Denissenkov (2010) have shown that the aspect ratio of salt fingers in RGB stars is rather $a \lesssim 1$. Given that the diffusion coefficient for thermohaline convection $D_{\rm th}$ is proportional to a^2, it turns out to be too inefficient for the RGB extra mixing.

In this work, we have chosen M13 (NGC 6205) as an exemplary instance of GCs with abundance anomalies of p-capture elements, because it is one of a few GCs that show the most extreme primordial abundance anomalies. We assume that its low-mass stars had been formed out of mixtures of the pristine gas and a varying fraction of material lost by a supermassive MS star with $M > 10^4\,M_\odot$, as described by Denissenkov & Hartwick (2014). Following Johnson & Pilachowski (2012), we use the O-Na anti-correlation for M13 stars to subdivide them into three populations according to the strength of their primordial abundance anomalies: a normal (or primordial) population is made of the pristine gas, while intermediate and extreme populations contain, respectively, 50% and 90% of material from the supermassive star mixed with the pristine gas. Then, we allow the low-mass stars belonging to the different populations to evolve from the zero-age MS to the RGB tip. The RGB extra mixing is modeled either using the thermohaline diffusion coefficient (equation 25) from Denissenkov (2010) with the salt-finger aspect ratios $a \gtrsim 7$ that provide the most efficient mixing or using the observationally constrained parametric prescription from Denissenkov & Pinsonneault (2008) and Denissenkov (2012) that employs the same mixing depth as in the thermohaline case, i.e. $\log_{10}(r_{\rm mix}/R_\odot) = -1.35$, and diffusion coefficient $D_{\rm mix} = \alpha K$, where K is the thermal diffusivity and $\alpha = 0.01-0.1$ is the free parameter. This simple model that focuses on the nucleosynthesis part (the first step) of the solution takes into account both the primordial and evolutionary abundance variations of the p-capture elements in GC stars. We compare its predictions with the relevant observational data not only for M13 but also for other GCs.

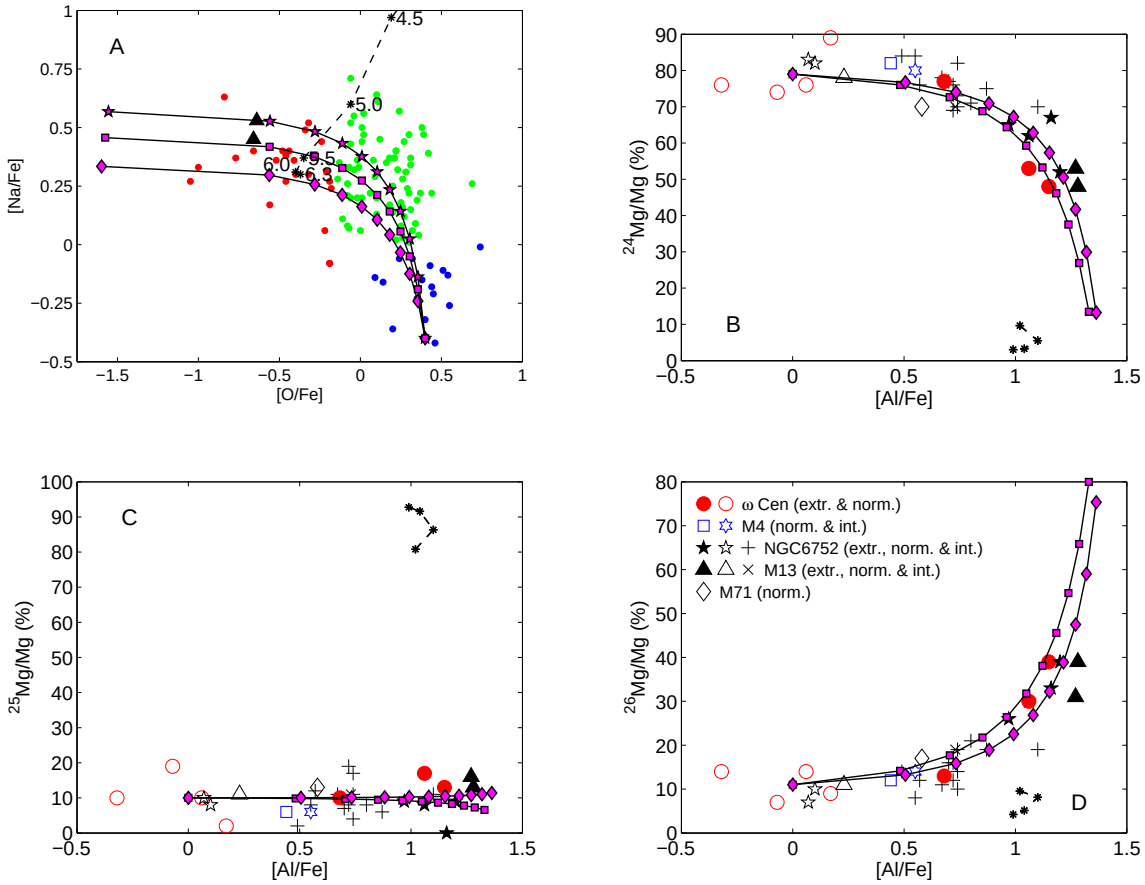

Figure 1. Panel A: the O-Na anti-correlation for the M 13 RGB stars (the blue, green and red circles) from Johnson & Pilachowski (2012) is compared with the dilution curves (the magenta star symbols, squares and diamonds connected by the solid black curves) obtained by mixing the abundances from the M 13 pristine gas (the lower-right ends of the curves) with a varying fraction (from 0% to 100%) of material from the supermassive MS stars with the masses $5 \times 10^4\,M_\odot$ (the star symbols), $6 \times 10^4\,M_\odot$ (the squares) and $7 \times 10^4\,M_\odot$ (the diamonds). The black asterisks connected by the dashed line are the theoretical data for the massive AGB stars with the indicated initial masses from Ventura & D'Antona (2009). Panels B, C and D: the Al abundances and Mg isotopic ratios for the 33 RGB stars from 5 GCs collected by Da Costa, Norris & Yong (2013) (the large single symbols, as identified in panel D) are compared with the theoretical predictions from the supermassive MS and massive AGB stars, as explained for panel A.

2 COMPUTATIONAL METHOD

The MS evolution of supermassive stars with $M > 10^4\,M_\odot$ is calculated using the revision 5329 of the stellar evolution code of MESA[1] (Paxton et al. 2011, 2013), as described by Denissenkov & Hartwick (2014). The evolution of low-mass stars with the RGB extra mixing modeled with the thermohaline diffusion coefficient $D_{\rm mix} = D_{\rm th}$ and parametric prescription $D_{\rm mix} = \alpha K$ is computed using the older MESA revision 3251 for which smoothing parameters were adjusted by Denissenkov (2010) to reproduce the results of his COMSOL high-resolution test simulations. Both codes are run with the same nuclear network that includes 31 isotopes from ^{1}H to ^{28}Si coupled by 60 reactions of the pp chains, CNO, NeNa and MgAl cycles. For solar composition, we use the elemental abundances of Grevesse & Sauval (1998) with the isotopic abundance ratios from Lodders (2003). The chemical composition of the pristine gas in M13 is obtained from the solar composition using $[{\rm Fe/H}]^2 = -1.53$ for the metallicity of M13 as a scaling factor and $[\alpha/{\rm Fe}] = +0.4$ for the abundances of α-elements (^{16}O, ^{20}Ne, ^{24}Mg etc.). We also assume $[{\rm Na/Fe}] = -0.4$ and the solar Mg isotopic ratios in the initial composition of the pristine gas because these values are suggested by the observational data (e.g., Fig. 1). With the MESA `kap` pre-processor we have generated opacity tables appropriate for our initial composition, i.e. the ones based on the Grevesse & Sauval (1998) solar abundances with $[\alpha/{\rm Fe}] = +0.4$, and employed them for all of our mixtures. The pre-processor uses the corresponding OPAL opacity tables (Iglesias & Rogers 1993, 1996) and low-temperature molecular opacities of Ferguson et al. (2005) as input data. For the convective mixing length, we have chosen the MESA solar calibrated parameter $\alpha_{\rm MLT} = 1.92$ in the Henyey, Vardya & Bodenheimer (1965) MLT prescrip-

[1] `http://mesa.sourceforge.net`

[2] We use the standard spectroscopic notation $[{\rm A/B}] = \log_{10}(N({\rm A})/N({\rm B})) - \log_{10}(N_\odot({\rm A})/N_\odot({\rm B}))$, where $N({\rm A})$ and $N({\rm B})$ are number densities of the nuclides A and B.

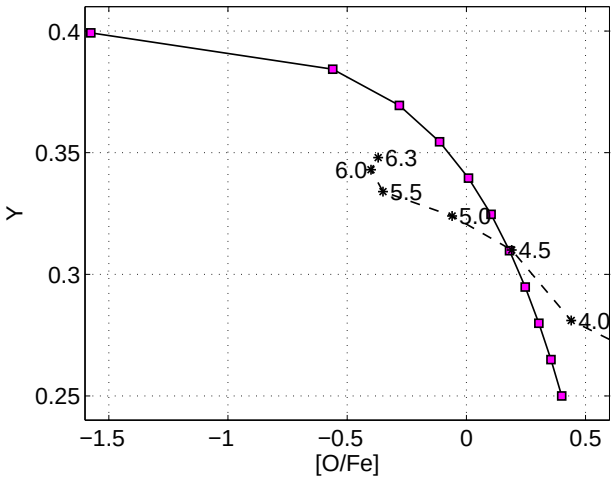

Figure 2. The same theoretical plot as in Fig. 1A, but for the He mass fraction Y. The dilution curves for the different supermassive MS star models are overlaying one another.

tion. Atmospheric boundary conditions are calculated in the approximation of Krishna Swamy (1966).

For M13 isochrone calculations, we have used the Victoria stellar evolution code (VandenBerg et al. 2012), because it treats both atomic diffusion and its counteracting turbulent mixing, whereas MESA code does not include the latter, which leads to an excessive depletion of the surface He abundance on the MS[3]. Therefore, in our MESA calculations of the evolution of low-mass stars we neglect atomic diffusion. This increases the effective temperature at the MS turn-off, but does not lead to important differences, except for Li, in the evolution of surface composition on the RGB as compared to the Victoria models, because the first dredge-up erases most of the surface abundance changes produced by atomic diffusion on the MS.

3 THREE POPULATIONS OF LOW-MASS STARS IN M 13

Following Denissenkov & Hartwick (2014), we calculate the evolution of supermassive MS stars with $M > 10^4\,M_\odot$ only until the He mass fraction at the surface and, because these stars are fully convective, also at the centre has reached the value $Y = 0.40$, which is close to the maximum He abundances reported in the present-day GC stars (Pasquini et al. 2011; King et al. 2012). The corresponding ages of the supermassive stars are less than 10^5 years. Their initial chemical composition is assumed to be that of the M13 pristine gas, which is equivalent to the composition of the M13 normal population in Table 1.

The filled blue, green and red circles in Fig. 1A represent, respectively, the normal (or primordial), intermediate and extreme populations of low-mass RGB stars in M 13, according to the selection criteria used by Johnson & Pilachowski (2012). Together, they form the O-Na anti-correlation which, like the other correlations between the p-capture elements and their isotopes, is usually interpreted as a result of mixing of the pristine gas with different fractions of material lost by massive stars that had taken place in the young GC, before those low-mass stars formed. In this interpretation, one end of a correlation, e.g. the lower-right end of the O-Na anti-correlation, gives abundances in the pristine composition ($[\mathrm{O/Fe}] \approx +0.4$ and $[\mathrm{Na/Fe}] \approx -0.4$ for M13), while the other end points towards abundances characteristic of the polluting star ($[\mathrm{O/Fe}] \lesssim -1$ and $[\mathrm{Na/Fe}] \approx +0.4$ for M 13).

The filled magenta star symbol, square and diamond at the left ends of solid black curves in Fig. 1A give the O and Na abundances in the MS stars with the masses $5 \times 10^4\,M_\odot$, $6 \times 10^4\,M_\odot$ and $7 \times 10^4\,M_\odot$ at $Y = 0.40$. The same symbols at other locations along the solid black curves show the results of these final abundances having been mixed with 10%, 20%,..., 90% and 100% of the O and Na abundances from the pristine gas. As the abundance mixtures representative for the normal, intermediate and extreme populations of stars in M13, we choose those with 0%, 50% and 90% of material from the supermassive stars (the first, sixth and tenth points on the solid black curves counting from their lower-right ends). We make such a discrete choice only for simplicity, while keeping in mind that, actually, there are no sharp boundaries between the three populations in Fig. 1A.

The different single symbols in Figs. 1B, 1C and 1D form the discernable dependences of the Mg isotopic ratios on the Al abundance. They represent observational data for 33 RGB stars from 5 GCs, including M13, that have recently been collected by Da Costa, Norris & Yong (2013). The filled magenta squares and diamonds connected by the solid black curves show the Al and Mg isotopic abundances for the same supermassive star models and mixtures as in Fig. 1A. The four panels in Fig. 1 illustrate the fact, already discussed by Denissenkov & Hartwick (2014), that the supermassive stars with $M > 10^4\,M_\odot$ reproduce all the primordial abundance variations of p-capture elements in GCs surprisingly well. The two filled black triangles in Fig. 1 are M13 stars that belong to the extreme population. From their locations in the four panels, we conclude that all the six abundances in these stars are consistent with the supermassive star hypothesis.

Denissenkov & Hartwick (2014) have noted that the success of the supermassive star models in the reproducing of the primordial abundance variations of the p-capture elements in GCs, including the Mg-Al anti-correlation, is not surprising, because these models have central temperatures in the right range for this, 74×10^4 K $\lesssim T_\mathrm{c} \lesssim 78 \times 10^6$ K, as was first shown by Denissenkov et al. (1998) in their "black box" solution and, later, independently confirmed by Prantzos, Charbonnel & Iliadis (2007). However, in both of the cited papers the H burning was considered to take place at a constant temperature and, as a result, the required final abundances were reached when less than 5% of H was consumed, which would not be sufficient to explain the He enhancements of up to $Y \approx 0.4$ measured in some GCs. In the fully convective supermassive MS stars, as much as 20% of H can be transformed into He, thus changing Y from its initial value 0.25 to 0.4, by the moment when the p-capture elements and their isotopes still have the required

[3] When very close to the same physics is assumed, the Victoria and MESA codes predict nearly identical evolutionary tracks and lifetimes for stars of a given mass and chemical composition (see VandenBerg et al. 2012).

Table 1. Initial mass fractions of isotopes used in our calculations

isotope	norm. pop.[a]	int. pop.[b]	extr. pop.[c]
^{1}H	0.748815	0.674238	0.614576
^{3}He	6.55411×10^{-5}	3.27706×10^{-5}	6.55416×10^{-6}
^{4}He	0.250000	0.324641	0.384353
^{7}Li	1.04586×10^{-9}	5.23263×10^{-10}	1.05187×10^{-10}
^{12}C	9.50177×10^{-5}	5.77948×10^{-5}	2.80165×10^{-5}
^{13}C	1.15310×10^{-6}	3.50972×10^{-6}	5.39501×10^{-6}
^{14}N	2.80540×10^{-5}	3.52988×10^{-4}	6.12936×10^{-4}
^{15}N	1.10507×10^{-7}	6.43548×10^{-8}	2.74331×10^{-8}
^{16}O	6.55465×10^{-4}	3.31200×10^{-4}	7.17876×10^{-5}
^{17}O	1.03384×10^{-7}	5.94662×10^{-8}	2.43319×10^{-8}
^{18}O	5.88641×10^{-7}	2.94323×10^{-7}	5.88687×10^{-8}
^{19}F	1.38744×10^{-8}	6.94144×10^{-9}	1.39506×10^{-9}
^{20}Ne	1.35740×10^{-4}	1.31317×10^{-4}	1.27779×10^{-4}
^{21}Ne	1.36018×10^{-7}	6.96419×10^{-8}	1.65412×10^{-8}
^{22}Ne	4.37084×10^{-6}	2.21363×10^{-6}	4.87857×10^{-7}
^{23}Na	1.16195×10^{-6}	4.76080×10^{-6}	7.63988×10^{-6}
^{24}Mg	4.37780×10^{-5}	2.34966×10^{-5}	7.27160×10^{-6}
^{25}Mg	5.77473×10^{-6}	3.70320×10^{-6}	2.04597×10^{-6}
^{26}Mg	6.60731×10^{-6}	1.36472×10^{-5}	1.92791×10^{-5}
^{27}Al	2.01755×10^{-6}	2.25630×10^{-5}	3.89994×10^{-5}
^{28}Si	5.69495×10^{-5}	5.86796×10^{-5}	6.00638×10^{-5}
^{56}Fe	3.92893×10^{-5}	3.92893×10^{-5}	3.92893×10^{-5}
^{58}Ni	4.33457×10^{-5}	4.33457×10^{-5}	4.33457×10^{-5}
[(C + N + O)/H]	−1.24	−1.19	−1.15

[a] The heavy-element mass fraction for this and the other two mixtures is $Z \approx 0.0011$.
[b]For the intermediate population, we assume a mixture of 50% of the abundances from the normal population with 50% of the abundances from our $6 \times 10^4\,M_\odot$ MS star model when its He abundance has increased to $Y = 0.40$.
[c]For the extreme population, we assume a mixture of 10% of the abundances from the normal population with 90% of the abundances from our $6 \times 10^4\,M_\odot$ MS star model when its He abundance has increased to $Y = 0.40$.

abundances. The filled magenta squares in Fig. 2 show the He and O abundances in the mixtures of the M13 pristine gas with different fractions of the material from the supermassive MS stars. According to this figure, the normal, intermediate and extreme populations of stars in M13 should have $Y = 0.25$, $Y = 0.32$ and $Y = 0.38$, respectively (see Table 1). These values agree with the He abundances in the blue horizontal branch stars in the GC NGC2808 measured by Marino et al. (2014).

4 SUPERMASSIVE MS STARS WITH $M > 10^4\,M_\odot$ VERSUS MASSIVE MS AND AGB STARS

4.1 The Al abundance and Mg isotopic ratios

Hydrogen burning in the convective cores of MS stars with $M \lesssim 10^3\,M_\odot$ that occurs at $T_c \lesssim 60 \times 10^6$ K as long as $Y < 0.40$ can result only in a marginal depletion of the ^{24}Mg abundance. Therefore, neither the fast-rotating massive MS stars with $20\,M_\odot \leqslant M \leqslant 120\,M_\odot$ (Decressin et al. 2007), nor the stars with $M = 20\,M_\odot$ in close binaries (de Mink et al. 2009), nor the very massive MS stars with $M \sim 10^3\,M_\odot$ (Sills & Glebbeek 2010), all of which have been proposed as the potential sources of the primordial abundance variations of the p-capture elements in GCs, can actually reproduce the observed patterns between the abundances of Al and Mg isotopes in Figs. 1B, 1C and 1D.

The four asterisks connected by the dashed line in Figs. 1B, 1C and 1D represent the theoretical data for the AGB stars with the initial masses $5.0\,M_\odot$, $5.5\,M_\odot$, $6.0\,M_\odot$ and $6.3\,M_\odot$ and heavy-element mass fraction $Z = 10^{-3}$, which is close to that of M13 stars, from Table 2 of Ventura & D'Antona (2009). They are located far away from the observed dependences which, on the other hand, are very well matched by the H-burning yields from the supermassive stars. Unlike the massive MS stars, the problem with the massive AGB stars is that the hot-bottom burning (HBB) of H in their convective envelopes occurs at too high temperatures, $T_{\rm HBB} \gtrsim 10^8$ K. In Fig. 3, we have plotted the (p,γ) reaction rates as functions of $T_9 \equiv T/10^9$ K for ^{24}Mg (the solid blue, black and red curves), ^{25}Mg (the dashed curves) and ^{16}O (the green curve) taken from the most recent experimental data compilations that we found using a Web interface[4] to the JINA REACLIB default library (Cyburt et al. 2010). This figure shows that at $T_9 \lesssim 0.06$ the reaction ^{24}Mg(p,γ) is more than three orders of magnitude slower than ^{16}O(p,γ). This explains why H burning in massive MS stars is not accompanied by the required depletion of ^{24}Mg. On the other hand, during the HBB in the massive AGB stars at $T_9 \gtrsim 0.1$ the rate of the reaction ^{24}Mg(p,γ) exceeds that of ^{16}O(p,γ). This should lead to a faster destruction of the most abundant magnesium isotope ^{24}Mg than ^{16}O, which could be a problem, because [O/Fe] usually exhibits much lower values than [Mg/Fe] in GCs (Denissenkov

[4] `https://groups.nscl.msu.edu/jina/reaclib/db/`

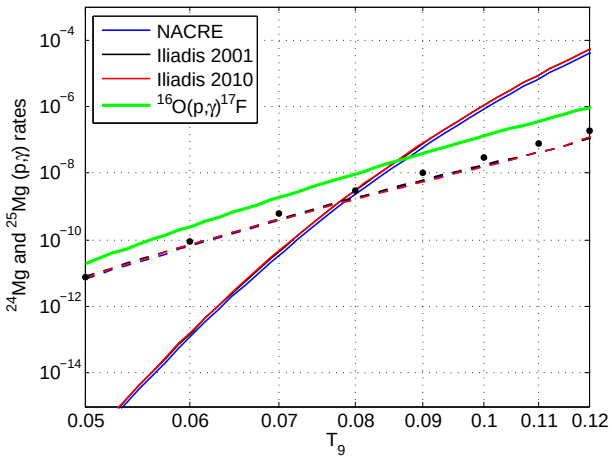

Figure 3. The (p,γ) reaction rates (cm^{3}s^{-1}mol^{-1}) for ^{24}Mg (the solid blue, black and red curves, the last two overlaying one another) and ^{25}Mg (the dashed curves of the same colors) from the different compilations indicated in the legend box (including Iliadis et al. (2001) and NACRE data from Angulo et al. (1999)), as well as for ^{16}O (the green curve) from Iliadis et al. (2010). These data have been found using a Web interface to the JINA REACLIB default library (Cyburt et al. 2010). The black circles are the most recent data for the reaction ^{25}Mg(p,γ)^{26}Al from Straniero et al. (2013).

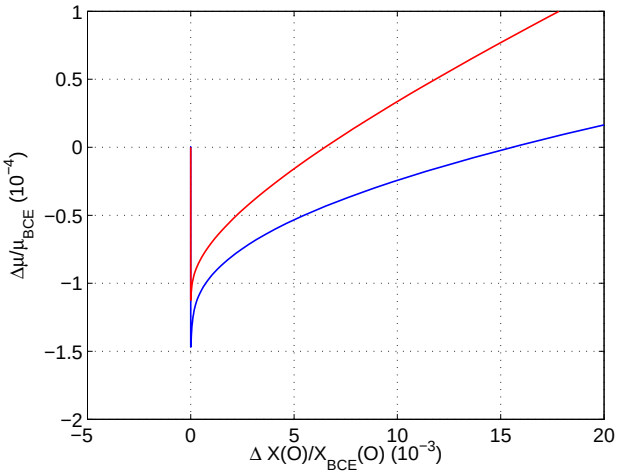

Figure 4. The relative changes of the mean molecular weight and oxygen abundance in the radiative zones of the normal (the blue curve) and extreme, i.e. He-rich, (the red curve) population RGB models with the masses $0.8\,M_\odot$ and $0.65\,M_\odot$, respectively, immediately above the bump luminosity. The μ ratio drops vertically in the vicinity of the H-burning shell (HBS), where the reaction ^{3}He(^{3}He,2p)^{4}He decreases μ locally, but the O abundance has not changed yet. Deeper in the HBS (to the right), the CNO cycle increases both μ and the relative deviation of the O abundance from its value at the bottom of the convective envelope (BCE).

& Herwig 2003), unless the ^{24}Mg destruction would lead to a commensurate accumulation of ^{25}Mg. This is exactly what happens in the massive AGB stars, because the reaction ^{25}Mg(p,γ) at $T_9 \gtrsim 0.1$ is slower than both the p-captures by ^{24}Mg and ^{16}O (Fig. 3). Only at $T_9 \approx 0.075$, which is close to the central temperatures in supermassive MS stars with $M > 10^4\,M_\odot$, we do find the right relative rates of the above three reactions, which guarantees that when ^{16}O is destroyed, a smaller amount of ^{24}Mg can also be burned, while the freshly produced ^{25}Mg will be rapidly converted into ^{26}Mg because its p-capture rate is higher than that of ^{24}Mg(p,γ). This explains why both the massive MS and AGB stars fail to reproduce the observed (anti-)correlations between the abundances of Al and Mg isotopes, while the H burning in the supermassive MS stars with $M > 10^4\,M_\odot$ does the work.

The black circles in Fig. 3 present the new rate for the reaction ^{25}Mg(p,γ)^{26}Al from Straniero et al. (2013), which is approximately two times as large as the older rates in the range of T_9 characteristic of the HBB in the massive AGB stars. Ventura, Carini & D'Antona (2011) estimated that with such the increase of this reaction rate they could obtain the [Mg/Fe] depletion and [Al/Fe] enhancement in a better agreement with observations. However, their Mg isotopic ratios in this case, ^{25}Mg/Mg = 90% and ^{26}Mg/Mg = 5.4%, as well as the ratios ^{25}Mg/Mg = 76% and ^{26}Mg/Mg = 5.6% from the super-AGB star with the initial mass $8\,M_\odot$ are still far away from the observed ones.

4.2 The O-Na anti-correlation

The minimum value of [O/Fe], that is still accompanied by a relatively high value of [Na/Fe] to fit the O-Na anti-correlation, obtained in the massive AGB models with the HBB is close to −0.5 (see the asterisks connected by the dashed line in Figs. 1A and 2). This presents another problem for the massive AGB star pollution hypothesis because some stars in M13 (the red circles to the left of [O/Fe] = −0.5), as well as stars in a few other GCs, possess much lower O abundances. To solve this problem, D'Antona & Ventura (2007) have proposed that the low-mass stars from the extreme population of GCs experience deeper extra mixing on the RGB than their counterparts from the normal population because the higher initial He abundance in the former (Fig. 2) should reduce the μ-discontinuity that prevents the RGB extra mixing from penetrating deep into the HBS. However, what really matters when one considers extra mixing in the radiative zone of an RGB star is its ability to overcome the restoring Archimedes force that is proportional to $\Delta\mu/\mu_{\rm BCE}$, where $\Delta\mu = \mu(r) - \mu_{\rm BCE}$, provided that $D_{\rm mix} \ll K$ which is true for the RGB extra mixing (see the next section). In Fig. 4, we compare the ratios $\Delta\mu/\mu_{\rm BCE}$ plotted as functions of a relative deviation of the local O mass fraction from its value at the BCE (we use the positive difference $\Delta X({\rm O}) = X_{\rm BCE}({\rm O}) - X({\rm O})$) in our $0.8\,M_\odot$ and $0.65\,M_\odot$ RGB models with the normal and extreme initial compositions from Table 1 immediately above the bump luminosity. Both quantities remain zero until we reach the vicinity of the HBS, where the μ-profile has the depression caused by the reaction ^{3}He(^{3}He,2p)^{4}He. There, the μ ratio drops vertically because there are no changes of the O abundance yet. When we move further to the right into the HBS, the H burning in the CNO cycle increases both $\Delta\mu$ and $\Delta X({\rm O})$. Fig. 4 shows that the $\Delta\mu/\mu_{\rm BCE}$ ratio increases faster in the extreme population RGB model, which means that its chemical structure does not facilitate the penetration of extra mixing deeper into the HBS and dredge up more material with a deficit in O, as compared to the normal population RGB model. Moreover, in order to attain

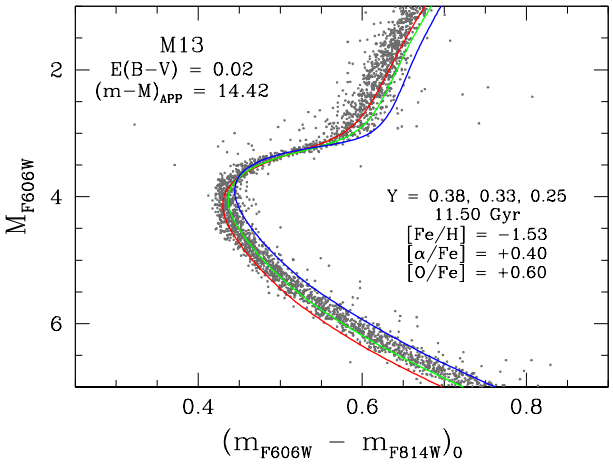

Figure 5. The three 11.5 Gyr isochrones generated with the Victoria stellar evolution code for the indicated combinations of Y, [Fe/H] and [α/Fe] that are close to those assumed in our normal ($Y = 0.25$, blue), intermediate ($Y = 0.33$, green) and extreme ($Y = 0.38$, red) compositions of low-mass stars in M 13 are compared with the M 13 HST ACS color-magnitude diagram.

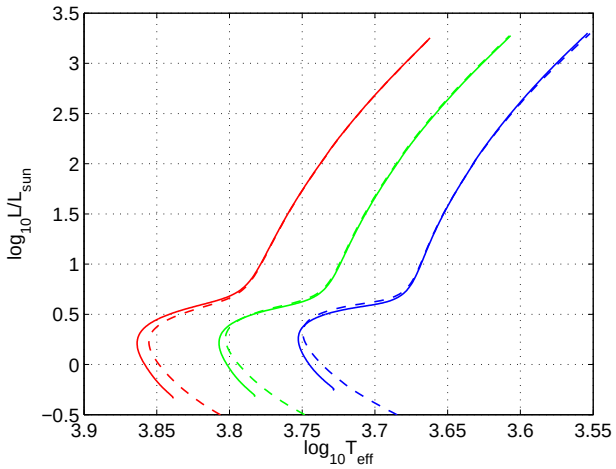

Figure 6. The isochrones (solid curves) for the normal (blue), intermediate (green) and extreme (red) populations of low-mass stars in M 13 and the stellar evolutionary tracks (dashed curves) of stars with the masses 0.8 $M_\odot$ (blue), 0.7 $M_\odot$ (green) and 0.65 $M_\odot$ (red) that have the corresponding initial compositions from Table 1 and matching red gian branches. The blue and red curves have been shifted by $\Delta \log_{10} T_{\rm eff} = \pm 0.05$ relative to the green curves.

the same level of the surface O depletion, if it is required by observations, the extreme population RGB star must have more powerful extra mixing, e.g. if the RGB extra mixing is driven by rotation then the extreme population stars in GCs must rotate faster than their normal population counterparts by some reason, which is difficult to understand.

In the hypothesis that proposes the supermassive stars with $M > 10^4\,M_\odot$ as the source of the primordial abundance variations in GCs, it is sufficient to assume that some low-mass stars in GCs were formed out of more than 90% of the material lost by these supermassive stars (Fig. 1A). We also note that the total CNO abundances in the M 13 RGB stars measured by Cohen & Meléndez (2005), namely the [(C+N+O)/H] ratios between -1.4 and -1.1 with the average value -1.23, are very close to those in our Table 1. Like massive MS stars, the supermassive stars destroy Li. However, we do not think that this is a serious problem at present because unevolved low-mass stars in some GCs, e.g. MS turn-off stars in 47 Tuc, show an order of magnitude variations in the Li abundance marginally correlating with [O/Fe] (Dobrovolskas et al. 2014).

5 THE EVOLUTIONARY ABUNDANCE VARIATIONS IN M13 RGB STARS

We have used the Victoria stellar evolution code to generate three 11.5 Gyr isochrones for the combinations of the initial He mass fraction, metallicity and α-element enhancement that are close to those assumed for the extreme, intermediate and normal populations of low-mass stars in M13 (Table 1). These isochrones are transformed to the HST ACS photometric system (using the colour–$T_{\rm eff}$ relations given by Casagrande & VandenBerg 2014) and compared with the HST CMD data for M13 in Fig. 5, for which we have selected the 100 stars in each 0.10 mag bin that have the smallest error bars on the observed magnitudes and colors. The individual evolutionary tracks of stars with the masses 0.65 $M_\odot$, 0.7 $M_\odot$ and 0.8 $M_\odot$ calculated for the first, second and third initial compositions, respectively, are found to have RGBs coinciding with the RGBs of their corresponding isochrones (Fig. 6). Therefore, we have chosen these masses as the initial ones for our study of the evolutionary abundance variations, caused by the RGB extra mixing, in the M13 low-mass stars belonging to the extreme, intermediate and normal populations, using for them the initial abundances from Table 1. In this study, we employ the revision 3251 of MESA instead of the Victoria code because the latter cannot model extra mixing on the upper RGB, although the Victoria code produces better isochrones than MESA because it accounts for the atomic diffusion and its counteracting turbulent mixing on the MS, which has not yet been implemented in the MESA code.

The red, green and blue curves in Fig. 7A show the evolution of the surface C abundance in the models representing the three populations of low-mass stars in M13, in which the RGB extra mixing has been modeled using the thermohaline diffusion coefficient (equation 25) from Denissenkov (2010). We have used the salt-finger aspect ratio $a = 7$ that gives the maximum possible depletion of [C/Fe] in these models. The open blue diamonds in Fig. 7A are M13 MS turn-off and subgiant stars for which the [C/Fe] values were determined by Briley, Cohen & Stetson (2002). They demonstrate a pattern characteristic of the equilibrium CNO cycle — the floor at [C/Fe] ≈ -0.8 (Denissenkov et al. 1998), which supports the idea that the primordial abundance variations in GC stars were produced in H burning at a sufficiently high temperature for the CNO cycle to reach equilibrium. The rest of the symbols in Fig. 7A, except the red star symbols that represent low-mass AGB stars, present the [C/Fe] data for RGB stars with $M_V < +0.8$ compiled by Smith & Briley (2006) from the literature. We have used $(m-M)_V = 14.42$ as the distance modulus for M13 and applied the correction Δ[C/Fe] $= +0.4$ to all of the RGB [C/Fe] values, as recommended in the cited paper. We see that the thermohaline

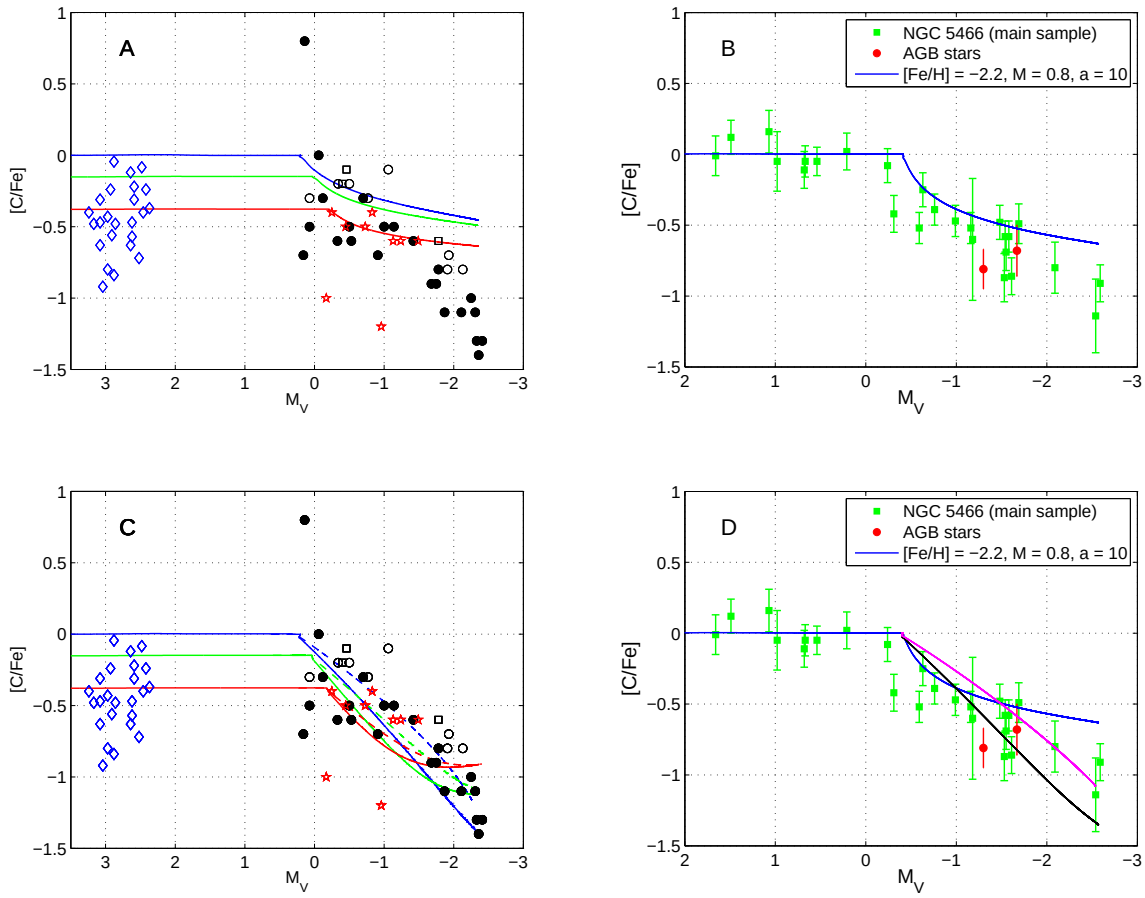

Figure 7. Panel A: the evolution of the surface C abundance in the stars with the masses $0.8\,M_\odot$ (blue), $0.7\,M_\odot$ (green) and $0.65\,M_\odot$ (red) and initial chemical compositions from the second, third and fourth columns of Table 1, respectively, calculated from the MS to the RGB tip. The RGB extra mixing is modeled using the thermohaline diffusion coefficient (equation 25) from Denissenkov (2010) with the salt-finger aspect ratio $a = 7$ that produces the maximum possible decrease of [C/Fe]. The results of these calculations are compared with the observational data for M 13 MS turn-off and subgiant stars (the open blue diamonds) and RGB stars (the other symbols, except the red star symbols which represent AGB stars) from Briley, Cohen & Stetson (2002). Panel B: the same as in panel A, but for the stars of the single stellar population GC NGC5466 observed by Shetrone et al. (2010) and $a = 10$. Panel D: The same as in panel B, but here we have also used the parametric prescription for the RGB extra mixing with the mixing depth $\log_{10}(r_{\rm mix}/R_\odot) = -1.35$ (same as for the thermohaline mixing) and diffusion coefficient $D_{\rm mix} = \alpha K$, where K is the radiative diffusivity and $\alpha = 0.02$ (magenta line) and 0.03 (black line). Panel C: the same as in panel D, but for the M 13 stars with the dashed and solid curves representing the cases of $\alpha = 0.02$ and 0.03.

convection driven by the ^{3}He burning produces shallow evolutionary declines of [C/Fe] incompatible with the observational data for the M13 RGB stars.

From Fig. 7B, the same conclusion can be made for the GC NGC 5466 stars studied by Shetrone et al. (2010), for which the value of $a = 10$ gives a maximum effect for the evolutionary depletion of [C/Fe] on the upper RGB (our defined maximal-mixing salt-finger aspect ratio slightly depends on the metallicity). This GC is unique because it does not appear to have any primordial abundance variations. Therefore, it can be used to calibrate the depth and rate of the RGB extra mixing. To eliminate the mixing depth as a free parameter, we assume that it is equal to the almost universal depth that we usually find for the ^{3}He-driven thermohaline convection in upper RGB models of different metallicities, i.e. $\log_{10}(r_{\rm mix}/R_\odot) = -1.35$. This depth guarantees that only the products of H burning in the CN branch of the CNO cycle are dredged up from the HBS to BCE, as indicated by observations. In the absence of a good candidate for the mechanism of the RGB extra mixing, we assume that it can be modeled as a diffusion process with a diffusion coefficient $D_{\rm mix}$ proportional to the radiative diffusivity

$$K = \frac{4acT^3}{3\kappa C_P \rho^2}, \qquad (1)$$

where a is the radiation constant, c the speed of light, κ is the Rosseland mean opacity, C_P is the specific heat at constant pressure and ρ is the density. This assumption makes sense as long as the RGB extra mixing operates on a thermal timescale, when the radiative heat diffusion facilitates it by reducing temperature contrasts between rising and sinking fluid parcels. In Fig. 7D, the magenta and black curves are obtained with $D_{\rm mix} = \alpha K$ for $\alpha = 0.02$ and 0.03, respectively. When we employ the same parameters of the RGB extra mixing in models of the M13 low-mass stars, we get very good agreement with the observational data (Fig. 7C), in spite of the fact that the two GCs have different metallicities, [Fe/H] = −1.53 for M13 and [Fe/H] = −2.2 for NGC 5466.

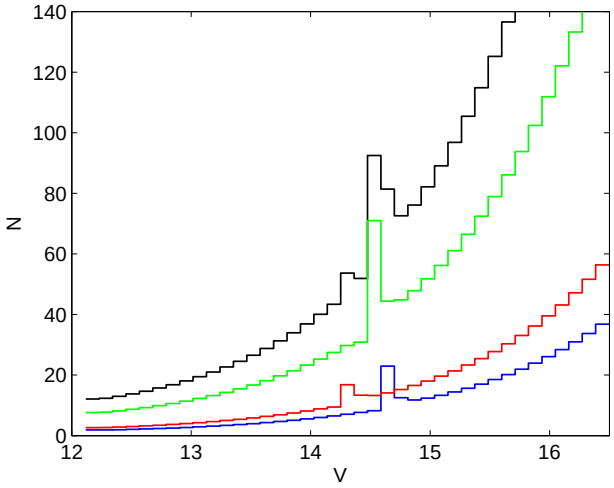

Figure 8. The theoretical differential luminosity functions for the evolutionary tracks from Fig. 7A (the blue, green and red histograms) constructed assuming that the three populations contribute 15%, 63% and 22% to the total population of stars in M 13, like in its O-Na anti-correlation (Johnson & Pilachowski 2012), as well as their composite luminosity function (the black histogram).

6 CMDS FOR THE THREE POPULATIONS OF LOW-MASS STARS IN M13

The color difference between our theoretical isochrones for the normal and extreme populations of low-mass stars in M13 in Fig. 5 is approximately as large as the width of its CMD observed with the HST ACS. Therefore, our assumption that M13 has the populations of low-mass stars with Y varying between 0.25 and 0.38 cannot be rejected on the basis of these photometric data[5]. This conclusion appears even more true when we take into consideration that both the extreme and normal populations are likely to be poorly presented in M13, as compared to its intermediate population. This possibility is supported by the fact that the O-Na anti-correlation for M13 in Fig. 1A includes 63% of the intermediate-population RGB stars, while the normal and extreme populations contribute only 15% and 22% (Johnson & Pilachowski 2012). Also, the M13 RGB stars with the most extreme abundance anomalies are predominantly located near the RGB tip, where the three isochrones almost converge. We remind the reader that our subdivision of the M13 low-mass stars into the three distinct populations is an approximation that has been made using the rather arbitrary selection criteria, while in fact both its O-Na anti-correlation and CMD display smooth distributions of stars.

From Fig. 7C, it is seen that the evolutionary tracks of the low-mass stars belonging to the different populations in M13 have slightly different bump luminosities, at which the RGB extra mixing starts to operate, increasing with Y. A differential luminosity function constructed for the normal population (the blue curve in Fig. 8) has a bump at $V \approx 14.7$ which is very close to its observed location in M13, $V \approx 14.75$, as reported by Sandquist et al. (2010), or $V \approx 14.77$, according to the most recent HST GC data analysis by Nataf et al. (2013). However, if the M13 low-mass stars represent a mixture of the three populations, then location and width of the bump depend on its relative strength and a number of stars in the different populations. It turns out that the former decreases when Y increases. The red, green and blue curves in Fig. 8 show the differential luminosity functions for the M13 three populations constructed assuming that they include 22%, 63% and 15% of all the M13 stars, like in its O-Na anti-correlation, while the black curve is their superposition. Given that the intermediate population is dominating in this mixture, the composite bump luminosity has shifted to $V \approx 14.6$. This analysis demonstrates that the observed location of the bump luminosity in a GC with multiple stellar populations can in principle be used to estimate their relative weights.

Monelli et al. (2013) have recently proposed a new photometric index, $c_{U,B,I} = (U-B)-(B-I)$, that should help reveal multiple stellar populations in GCs more easily. They have used this index to identify three populations of RGB stars in M13, members of which occupy different parts of its O-Na anti-correlation. In Fig. 9, we have plotted RGBs of our three models with the initial masses $0.8\,M_\odot$, $0.7\,M_\odot$ and $0.65\,M_\odot$ and chemical compositions from the second, third and fourth columns of Table 1, respectively, using the same photometric colors and panel formats as in Fig. 5 of Monelli et al. (2013), where the corresponding observational data were presented for the GC M13 (NGC 6205). Note that in this figure we have changed our population color coding, so that the green, red and blue curves now correspond to the normal, intermediate and extreme populations of stars in M13, as in the cited paper. The main difference between our and their plots is that the curves in our left panel have the opposite order. We have found the most likely explanation of this in the paper of Sbordone et al. (2011), who show that the enhanced abundance of N in the population of stars polluted by the products of H burning (the intermediate and primordial populations in our case) leads to a significant increase of the U magnitude because of the higher concentrations of the CN and NH molecules in these stars that absorb more light in the U band. To compensate for this effect, the U magnitude should be increased by an amount that depends on the effective temperature, gravity and detailed chemical composition. Sbordone et al. (2011) have calculated the required corrections for U, as well as similar bolometric corrections (BCs) for other photometric bands, using synthetic spectra for low-mass stars with chemical compositions typical for an intermediate-metallicity GC with multiple stellar populations at different evolutionary phases from the MS to the RGB tip. For the range of the V magnitude in Fig. 9, the BCs are important only for the U magnitude. When we apply them to the extreme-population RGB in the left panel, the solid blue curve is transformed into the dashed blue one, so that we get the right arrangement of the green and blue curves. The other difference is that the RGBs of our normal and extreme population models have larger separations in the $V-B$ and $B-I$ colors. This is probably caused by the fact that the M13 extreme population in the classification of Monelli et al. (2013) is actually

[5] The implications of high helium abundances and/or a wide range in Y for the horizontal branch of M13 will be considered in a separate paper (P. Denissenkov et al., in preparation). Some studies (e.g. Catelan et al. 2009) have argued in support of a normal helium content for this cluster, while others have estimated $Y_{\rm max} \approx 0.31$ for M13 HB stars (e.g. Dalessandro et al. 2013).

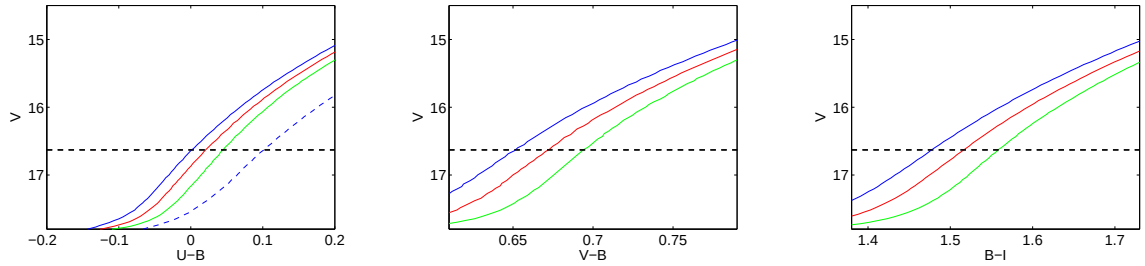

Figure 9. The lower RGBs of our three assumed populations of M 13 stars plotted for the same colors and in the same format as in the middle panel of Fig. 5 in Monelli et al. (2013). Note that now the green, red and blue curves correspond to the normal, intermediate and extreme populations, like in the paper of Monelli et al. (2013). The dashed blue curve in the left panel is obtained from the solid blue curve with the bolometric corrections to U from Sbordone et al. (2011) that take into account the larger N abundance in the extreme population.

closer to our intermediate population in the V range shown in Fig. 9, as suggested by the lower panel of their Fig. 15. Therefore, to compare our plots with theirs, we have to only keep our normal and intermediate populations, their intermediate populations falling between them, in which case the separations become comparable.

7 CONCLUSION

In this paper, we have elaborated on the hypothesis, recently proposed by Denissenkov & Hartwick (2014), that the primordial abundance anomalies of the p-capture elements and their isotopes in GC stars had been produced during a short time ($\sim 10^5$ years) of H burning in the fully convective supermassive MS stars with $M > 10^4\,M_\odot$. Because such stars are supported against the force of gravity almost entirely by the radiation pressure, they are subject to the diffusive mode of the Jeans instability, which develops on all length scales and on a timescale comparable to the lifetime of the supermassive stars (Thompson 2008; Denissenkov & Hartwick 2014). Therefore, those stars might have fallen apart (fragmented) soon after they had formed, by a moment when only a small fraction of H was transformed into He, as we have assumed. It is out of the scope of the present paper to discuss how the supermassive stars had formed in the young GCs (the two possible formation scenarios are briefly reviewed by Denissenkov & Hartwick 2014), or how they had lost their mass and how that mass, polluted with the products of H burning, had been mixed with the GC pristine gas before the low-mass stars formed out of that mixture. Here, we have focused on the nucleosynthesis part of the solution.

We have shown that among the massive star candidates for the origin of the primordial abundance anomalies in GCs proposed so far, such as the massive MS stars (rapidly rotating, members of binary systems, or as massive as $\sim 10^3\,M_\odot$), massive AGB stars and supermassive MS stars with $M > 10^4\,M_\odot$, only the latter have the right temperatures of H burning in the range $74{\times}10^6\ \mathrm{K} \lesssim T_\mathrm{c} \lesssim 78{\times}10^6$ K for the successful reproduction of the (anti-)correlations between the Al and Mg isotopic abundances, that have now been found to be common for 5 GCs.

The agreement between the primordial abundance anomalies of the p-capture elements in GCs and their corresponding abundance variations in the mixtures composed of the pristine GC material and H-burning yields from the supermassive MS stars with $M > 10^4\,M_\odot$ is so good that it is worth trying to (1) use such mixtures, e.g. those from Table 1, as the initial compositions for low-mass star models that are supposed to belong to different populations of stars in a GC with multiple stellar population, (2) allow these models to evolve and (3) see how various physical assumptions, e.g. the parameters of the RGB extra mixing and mass loss, will affect their surface chemical composition and evolution on the CMD in comparison with observational data. We have tried this for the GC M 13 (NGC6205) and found that the evolutionary decline of the C abundance in its upper RGB stars cannot be explained by the ^{3}He-driven thermohaline convection. We have estimated the depth and rate of the RGB extra mixing that allow to reproduce the observational decrease of [C/Fe] with M_V. They turn out to have the same values for both M 13 that has the most extreme primordial abundance anomalies and NGC5466 that does not have such anomalies. The fact that the two GCs also have different metallicities supports the old idea about the universality of the RGB extra mixing (e.g. Denissenkov & VandenBerg 2003). However, we are still missing the understanding of its physical mechanism. Given that the supermassive stars considered by Denissenkov & Hartwick (2014) are hypothetical objects and that neither the massive MS stars nor the massive AGB stars can reproduce the (anti-)correlations between the Al and Mg isotopic abundances in GCs, the source of the primordial abundance variations in GCs also remains uncertain. This leaves us with a problem with two unknowns.

ACKNOWLEDGMENTS

This research has been supported by the National Science Foundation under grants PHY 11-25915 and AST 11-09174. This project was also supported by JINA (NSF grant PHY 08-22648). Falk Herwig and Don VandenBerg acknowledge funding from Natural Sciences and Engineering Research Council of Canada. Pavel Denissenkov is grateful to the staff of the Max-Planck-Institut für Astrophysik, where this project was completed, for their warm hospitality. We thank M. Salaris who has generously provided us with the Sbordone et al. bolometric corrections.

REFERENCES

Angulo C. et al., 1999, Nuclear Physics A, 656, 3
Briley M. M., Cohen J. G., Stetson P. B., 2002, ApJ, 579, L17
Briley M. M., Harbeck D., Smith G. H., Grebel E. K., 2004, AJ, 127, 1588
Briley M. M., Smith V. V., Suntzeff N. B., Lambert D. L., Bell R. A., Hesser J. E., 1996, Nature, 383, 604
Cannon R. D., Croke B. F. W., Bell R. A., Hesser J. E., Stathakis R. A., 1998, MNRAS, 298, 601
Casagrande L., VandenBerg D. A., 2014, MNRAS, 444, 392
Catelan M., Grundahl F., Sweigart A. V., Valcarce A. A. R., Cortés C., 2009, ApJ, 695, L97
Charbonnel C., Zahn J.-P., 2007, A&A, 467, L15
Cohen J. G., Meléndez J., 2005, AJ, 129, 303
Cyburt R. H. et al., 2010, ApJS, 189, 240
Da Costa G. S., Norris J. E., Yong D., 2013, ApJ, 769, 8
Dalessandro E., Salaris M., Ferraro F. R., Mucciarelli A., Cassisi S., 2013, MNRAS, 430, 459
D'Antona F., Gratton R., Chieffi A., 1983, Mem. Societa Astronomica Italiana, 54, 173
D'Antona F., Ventura P., 2007, MNRAS, 379, 1431
de Mink S. E., Pols O. R., Langer N., Izzard R. G., 2009, A&A, 507, L1
Decressin T., Meynet G., Charbonnel C., Prantzos N., Ekström S., 2007, A&A, 464, 1029
Denissenkov P. A., 2010, ApJ, 723, 563
Denissenkov P. A., 2012, ApJ, 753, L3
Denissenkov P. A., Da Costa G. S., Norris J. E., Weiss A., 1998, A&A, 333, 926
Denissenkov P. A., Hartwick F. D. A., 2014, MNRAS, 437, L21
Denissenkov P. A., Herwig F., 2003, ApJ, 590, L99
Denissenkov P. A., Pinsonneault M., 2008, ApJ, 679, 1541
Denissenkov P. A., VandenBerg D. A., 2003, ApJ, 593, 509
Dobrovolskas V. et al., 2014, A&A, 565, A121
Eggleton P. P., Dearborn D. S. P., Lattanzio J. C., 2006, Science, 314, 1580
Ferguson J. W., Alexander D. R., Allard F., Barman T., Bodnarik J. G., Hauschildt P. H., Heffner-Wong A., Tamanai A., 2005, ApJ, 623, 585
Gratton R. G., Bonifacio P., Bragaglia A., et al.,, 2001, A&A, 369, 87
Gratton R. G., Carretta E., Bragaglia A., 2012, Astronomy and Astrophysics Reviews, 20, 50
Grevesse N., Sauval A. J., 1998, Space Science Reviews, 85, 161
Henyey L., Vardya M. S., Bodenheimer P., 1965, ApJ, 142, 841
Iglesias C. A., Rogers F. J., 1993, ApJ, 412, 752
Iglesias C. A., Rogers F. J., 1996, ApJ, 464, 943
Iliadis C., D'Auria J. M., Starrfield S., Thompson W. J., Wiescher M., 2001, ApJS, 134, 151
Iliadis C., Longland R., Champagne A. E., Coc A., Fitzgerald R., 2010, Nuclear Physics A, 841, 31
Johnson C. I., Pilachowski C. A., 2012, ApJ, 754, L38
King I. R. et al., 2012, AJ, 144, 5
Kraft R. P., 1979, ARA&A, 17, 309
Kraft R. P., 1994, PASP, 106, 553
Krishna Swamy K. S., 1966, ApJ, 145, 174
Lodders K., 2003, ApJ, 591, 1220
Marino A. F. et al., 2014, MNRAS, 437, 1609
Milone A. P. et al., 2012, ApJ, 744, 58
Monelli M. et al., 2013, MNRAS, 431, 2126
Nataf D. M., Gould A. P., Pinsonneault M. H., Udalski A., 2013, ApJ, 766, 77
Pasquini L., Mauas P., Käufl H. U., Cacciari C., 2011, A&A, 531, A35
Paxton B., Bildsten L., Dotter A., Herwig F., Lesaffre P., Timmes F., 2011, ApJS, 192, 3
Paxton B. et al., 2013, ApJS, 208, 4
Prantzos N., Charbonnel C., Iliadis C., 2007, A&A, 470, 179
Sandquist E. L., Gordon M., Levine D., Bolte M., 2010, AJ, 139, 2374
Sbordone L., Salaris M., Weiss A., Cassisi S., 2011, A&A, 534, A9
Shetrone M., Martell S. L., Wilkerson R., Adams J., Siegel M. H., Smith G. H., Bond H. E., 2010, AJ, 140, 1119
Sills A., Glebbeek E., 2010, MNRAS, 407, 277
Smith G. H., Briley M. M., 2006, PASP, 118, 740
Straniero O. et al., 2013, ApJ, 763, 100
Thompson T. A., 2008, ApJ, 684, 212
VandenBerg D. A., Bergbusch P. A., Dotter A., Ferguson J. W., Michaud G., Richer J., Proffitt C. R., 2012, ApJ, 755, 15
Ventura P., Carini R., D'Antona F., 2011, MNRAS, 415, 3865
Ventura P., D'Antona F., 2009, A&A, 499, 835